

Research Article

Deciphering the concentration-dependent modulation effect of CT16 on the human $\alpha 7$ nicotinic receptor: Insights from molecular dynamics simulation

Chuanbo Wang, Jinfei Mei, Mengke Jia, Sajjad Ahmad, Zijian Liu, Hongqi Ai*

School of Chemistry and Chemical Engineering, University of Jinan, Jinan 250022, China

ARTICLE INFO

Keywords:

CT16 peptides
 $\alpha 7$ nAChR receptor
Concentration-dependent modulation
Allosteric mechanism
Implications for therapeutic strategies

ABSTRACT

Alzheimer's disease (AD) is closely linked to the accumulation of amyloid-beta peptides ($A\beta$), which impair synaptic plasticity and contribute to cognitive decline. Among the fragments of $A\beta$, the CT16 peptide (the equivalent of $A\beta 16$, derived from soluble amyloid precursor protein α , sAPP α) has been shown to interact with the $\alpha 7$ nicotinic acetylcholine receptor ($\alpha 7$ nAChR), potentially enhancing synaptic plasticity. However, the concentration-dependent modulation of CT16 on $\alpha 7$ nAChR and its underlying mechanisms remain poorly understood. We employ molecular dynamics simulations to investigate how varying concentrations of CT16 affect the conformation and function of the $\alpha 7$ nAChR, and establishes the proportional relationship between CT16 concentration and $\alpha 7$ nAChR receptor function regulation at the molecular level, finding a stoichiometric ratio of 1:3 for maximum activation of $\alpha 7$ nAChR by CT16, and establishing the first demonstration that the constriction geometry of the pore within extracellular domain (specifically its minimal cross-sectional area) serves as the dominant structural determinant for ion permeation pathways at stoichiometric CT16: $\alpha 7$ nAChR binding (1:1 ratio), a phenomenon contrasting sharply with scenarios at higher ratios (CT16: $\alpha 7$ nAChR > 1:1). The presence of CT16 not only induces significant conformational changes, stabilizes specific receptor regions, but also modulates the ion channel's pore geometry in a concentration-dependent manner. These findings shed light on the potential role of CT16 in regulating synaptic plasticity and offer theoretical insights into its dual role as a positive allosteric modulator at low concentrations and an inhibitor at higher concentrations, which may have implications for therapeutic strategies targeting $\alpha 7$ nAChR in AD and other neurodegenerative diseases.

1. Introduction

Amyloid-beta peptide ($A\beta$) is intimately associated with the pathology of Alzheimer's disease (AD), manifesting as cognitive dysfunction and progressive memory loss [1]. The aggregation of $A\beta$ can directly impair synaptic plasticity, contributing to the onset of AD. $A\beta$ is derived from amyloid precursor protein (APP) through the cleavage by β - and γ -secretases (Fig. 1(b)), containing approximately 37–49 residues, with $A\beta 40$ and $A\beta 42$ being the most abundant [2]. The aggregation of $A\beta 42$ oligomers has been demonstrated to directly impair synaptic plasticity. Soluble APP alpha (sAPP α , the 1–612 fragment of APP) and C-terminal fragment alpha (CTF- α , the 613–695 fragment of APP) are products of the APP structural domain (1–695 of APP) cleaved and hydrolyzed by α -secretase. CTF- α can be further cleaved by γ -secretase to produce extracellular P3 fragments (truncated fragments, $A\beta 17$ –40, $A\beta 17$ –42) and the intracellular domain AICD (APP Intracellular Domain) [3–5] that ultimately flows into the cytoplasm [6]; whereas sAPP α can be cleaved further by β -secretase to yield CT16 (the 597D-K612 fragment), which cor-

responds to the C-terminal 16 amino acid residue fragment of sAPP α [7]. This is just the N-terminal 16-residue fragment of exogenous $A\beta 40/A\beta 42$ (renumbered as 1D-K16, $A\beta 16$). Extensive researches have confirmed that sAPP α plays a crucial role in the neuroprotection of APP and the modulation of synaptic plasticity [8,9]. sAPP β , which lacks the CT16 present in sAPP α , has been shown to be sufficient to promote long-term potentiation (LTP), a process that depends on the functional $\alpha 7$ nicotinic acetylcholine receptor ($\alpha 7$ nAChR) [10]. This suggests that CT16 acts as an effective fragment to interact with $\alpha 7$ nAChR. Impairments in the function of $\alpha 7$ nAChR are associated with a variety of neuropsychiatric and neurological disorders, such as schizophrenia and AD [11,12]. For neuroprotective effects, the N-terminal 16-peptide fragment of $A\beta$ ($A\beta 16$), which is also the CT16 fragment of sAPP α , is the most abundant $A\beta$ fragment found in human cerebrospinal fluid (CSF) [13,14]. Studies have indicated that CT16 can enhance synaptic plasticity and memory formation by increasing the release of presynaptic neurotransmitters at physiological concentrations, and it regulates the synaptic vesicle (SV) pool by phosphorylating the nicotinic receptor $\alpha 7$ nAChR, thus exerting

* Corresponding author.

E-mail address: chm_aihq@ujn.edu.cn (H. Ai).

<https://doi.org/10.1016/j.chphma.2025.07.001>

Received 16 March 2025; Received in revised form 30 June 2025; Accepted 16 July 2025

Available online 10 August 2025

2772-5715/© 2025 The Authors. Publishing Services by Elsevier B.V. on behalf of KeAi Communications Co. Ltd. This is an open access article under the CC BY license (<http://creativecommons.org/licenses/by/4.0/>)

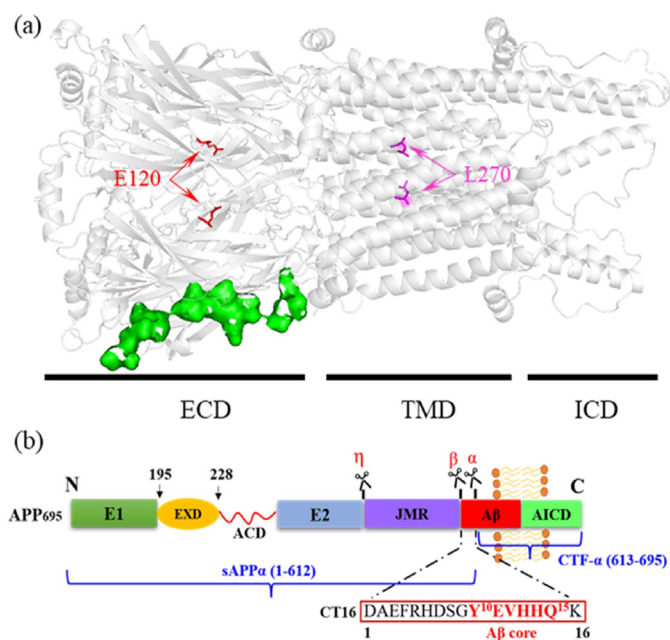


Fig. 1. (a) Structures of the $\alpha 7$ nAChR receptor (grey) bound to CT16 (green), in which E120 is shown in red, L270 in magenta. (b) Various functional domains of APP695, in which CT16 is highlighted and residues are displayed.

neuroprotective functions similar to full-length sAPP α [15–17]. The latest research further revealed that the A β 16, rather than the C-terminal A β 17–40/42, possesses all the regulatory functions of a high-quality A β 1–40/42 and is a sufficient and necessary condition for modulating presynaptic recycling [17,18]. Therefore, CT16 shares similar physiological functions with A β 1–40/42 when binding to the $\alpha 7$ nAChR.

The $\alpha 7$ nAChR is composed of five identical subunits surrounding a central axis, forming a typical pentameric structure (Fig. 1(a)). The $\alpha 7$ nAChR in complex with the antagonist α -bungarotoxin (α -bgt) exhibits a resting-like closed channel conformation, while binding to the agonist epibatidine and the positive allosteric modulator PNU-120596 result in a stable activated open channel conformation. It will form a desensitized closed channel conformation when complexed with epibatidine alone. Significant conformational changes occur among these three states. Cryo-electron microscopy structures have successfully captured the $\alpha 7$ nAChR molecular PDB structures in these different states and the distinct binding domains accommodated with their ligands [19,20]. In the resting state, the aperture of the lipid-bound $\alpha 7$ nAChR is located at the position of residue L270 (Fig. 1(a)) in the M2 helix of the transmembrane domain (TMD), with a radius of approximately 1.4 Å, which is too narrow to pass for hydrated cations, indicating a closed channel conformation [21]. In this structure, the molecular architecture is relatively compact, with the helices within the TMD maintaining a state of relative immobility, and the arrangement of amino acid side chains within the channel rendering the pore closed [20]. When bound by a ligand(s), such as acetylcholine (ACh), the conformation of the receptor will change, leading to the opening of the channel pore (with a radius at L270 greater than 1.4 Å) and the activation of the receptor [20,21]. Desensitization typically occurs after continuous or prolonged activation by the ligand, which will result in the channel non-permeable again although the receptor is still bound by the ligand [21]. The primary binding site for selective ligands was identified at the interface between the main chain of the extracellular domain (ECD) of $\alpha 7$ nAChR and the complementary subunit [22,23]. Each $\alpha 7$ nAChR subunit comprises a N-terminal ECD, which serves as the primary ligand-binding region of the receptor and is responsible for recognizing and binding acetylcholine and other ligands [12]; a TMD, consisting of several α -helical transmembrane segments that form the main structure of the ion channel,

and a small ligand-binding region (such as ivermectin), where conformational changes in the TMD upon ligand binding lead to the opening of the ion channel, allowing the passage of ions such as sodium and calcium through the membrane; and a large, flexible intracellular loop domain (ICD), primarily involved in the internal signaling and regulation of the receptor [24]. This region can be regulated by post-translational modifications (such as phosphorylation) to modulate the function and expression of the receptor [25]. The $\alpha 7$ nAChR responds to ACh or its hydrolysis product, choline, inducing rapid cation influx [26]. Therefore, this receptor is one of the promising therapeutic targets for the treatment of cognitive disorders and certain cancers, particularly those related to AD, schizophrenia, and depression [27–30] and becoming a novel drug target for restoring cognitive function in patients with AD [31].

Multiple studies have demonstrated that A β 42 directly binds to $\alpha 7$ nAChR, and acts as a direct agonist or antagonist of $\alpha 7$ nAChR in a concentration-dependent manner [32–34]. A consensus exists that low concentrations of A β 42 (picomolar) activate $\alpha 7$ nAChR, acting as a positive allosteric modulator, while higher concentrations (micromolar) exert an inhibitory effect [35–37], triggering neurotoxic effects and leading to synaptic damage, behavioral deficits, and apoptosis [38]. The dual roles, an agonist and a negative modulator, especially the latter induced by the higher A β concentrations may lead to cholinergic signaling deficits and could be involved in the onset and progression of AD [39].

Conformational studies indicate that low concentrations of soluble A β 42 modulate $\alpha 7$ nAChR through a biphasic mechanism [40]. At nanomolar levels, A β 42 binds to the ECD of $\alpha 7$ nAChR, inducing asymmetric subunit rearrangements that destabilize the closed state and transiently stabilize an open-channel conformation [33,40]. Upon increasing A β 42 concentrations by a thousand fold to the picomolar range, this activation is mediated [39]. In contrast, micromolar concentrations of A β 42 disrupt inter-subunit coupling and promoting desensitized non-conductive states [39]. Therefore, these conformational changes and A β 42 concentrations come into close association, underlying the study on the structure-function relationship of $\alpha 7$ nAChR-A β complex, benefiting us to raise following questions. What the specific concentration of CT16 can provide optimal activation or begin to inhibit $\alpha 7$ nAChR, and what is the allosteric mechanism underlying these modulatory effects?

2. Methodology

2.1. Model preparation

The structure of $\alpha 7$ -apo (PDB: 7eki) [21] is taken as the $\alpha 7$ nAChR model by retaining only the full protein coordinate. To ensure biological relevance, the simulated stoichiometries of $\alpha 7$ nAChR to CT16, ranging from 1:1 to 1:5, were calibrated using A β concentrations observed in Alzheimer's disease microenvironments. Experimental studies have shown that A β 1–42 levels in the cerebrospinal fluid of AD patients typically fall within the range of 0.04 to 0.1 μ M [41,42], while synaptic A β oligomers can accumulate to much higher local concentrations, reaching up to 10 μ M due to spatial confinement. Considering a typical neuronal membrane receptor density of approximately 1000 receptors per square micrometer, these concentration ranges correspond to ligand-to-receptor ratios from 1:1 to 5:1. This alignment confirms that our simulated systems effectively represent the pathophysiological conditions spanning from early to advanced stages of Alzheimer's disease. CT16 dimerization may occur at high concentrations and have conducted additional simulations to explore the dimer binding. To investigate this, the monomeric conformation was first docked. Then five CT16 ligands and the dimer ligands were successively docked onto it through the HDock 2.0 website [43] and five $\alpha 7$ nAChR-(CT16) $_i$ ($i = 1, 2, 3, 4,$ and 5) complexes were sequentially selected based on the docking score, prioritizing those that aligned with the ligand-protein binding positions as the evaluation criteria and termed them as $\alpha 7$ -1, $\alpha 7$ -2, $\alpha 7$ -3, $\alpha 7$ -4, and $\alpha 7$ -5, respectively. The five $\alpha 7$ - i ($i = 1, 2, 3, 4,$ and 5) complexes and

$\alpha 7$ -apo (resting state) were prepared for submitting to the "CHARMM-GUI" website [44] to build models of all-atom molecular dynamics (MD) simulations.

2.2. Molecular dynamics simulation protocol

All the proteins were surrounded by cubic periodic bounding boxes with initial dimensions of $120 \text{ \AA} \times 120 \text{ \AA} \times 120 \text{ \AA}$, where the distance between the complexes and the box boundaries was set as 10 \AA , and the TIP3P water model was employed. Subsequently, 0.15 M NaCl was added for mimicking the physiological condition [45]. Energy minimization was performed using the steepest descent algorithm with a convergence threshold of $1000 \text{ kJ}\cdot\text{mol}^{-1}\cdot\text{nm}^{-1}$ (Emtol) to eliminate atomic clashes. To further stabilize the system, a 1.0 ns equilibration run was propagated under the NVT ensemble, followed by 1.0 ns production run in the NPT ensemble. The constant temperature 310 K was maintained using Nose-Hoover ($\tau_T = 1.0 \text{ ps}$) [46] in the NVT ensemble and the constant pressure was maintained at 1 bar using the Parrinello-Rahman ($\tau_P = 5.0 \text{ ps}$) [47] pressure coupling algorithm in the NPT ensemble. The integration time step was set to 2 fs for all MD simulations [48]. System coordinates and energies were stored in trajectories at 2-ps intervals for subsequent analysis. In the whole simulation process, LINCS algorithm [49] was used to constrain the bond length of hydrogen atom, STEETLE algorithm [50] was used to constrain the geometry, and PME algorithm at 1.2 nm cutoff was used to calculate the long-range electrostatic interaction [51,52]. To conserve computational resources, three replicate MD trajectories were run for the $\alpha 7\text{-}1/\alpha 7\text{-}3$, in which the three initial structures for these replicates were derived from the snapshots at $30, 60, \text{ and } 100 \text{ ps}$, respectively, during the 1.0 ns production run in the NPT ensemble, as multi-replicate sampling from early-equilibrium snapshots was confirmed to enhance conformational coverage without requiring extended simulation durations [53]. All these all-atom MD simulation were performed by using GROMACS 2020.4 software [46] in combination with CHARMM36m force field [54].

In the hydrogen bond calculations, a cutoff distance of 0.35 nm and a bond angle cutoff of 30° were set [55,56]. HOLE was used to estimate pore diameters [57], structural visualization and figure preparation were conducted using software packages Chimera [58], VMD [59], and PYMOL [60].

2.3. Calculation of binding free energy

Molecular Mechanics Poisson-Boltzmann Surface Area (MMPBSA) is employed to perform binding free energy (ΔG_{bind}) calculation, which is a widely utilized approach for post-processing molecular dynamics (MD) trajectories to estimate binding free energies [61], with the specific formula as follows [62,63],

$$\Delta G_{\text{bind}} = \Delta H - T\Delta S \approx \Delta E_{\text{MM}} + \Delta G_{\text{sol}} - T\Delta S, \quad (1)$$

$$\Delta E_{\text{MM}} = \Delta E_{\text{ele}} + \Delta E_{\text{vdW}}, \quad (2)$$

$$\Delta G_{\text{sol}} = \Delta E_{\text{pb}} + \Delta E_{\text{np}}, \quad (3)$$

$$\Delta E_{ij}^{\text{ele}} = ij \frac{q_j q_i}{4\pi\epsilon_0\epsilon_{\text{in}}r_{ij}}, \quad (4)$$

$$\Delta G_{\text{SA}} = \gamma \cdot \text{SASA} + b \quad (5)$$

$$\Delta G_{\text{bind}/\text{fitted}} = 0.05402(\Delta E_{\text{COU}} + \Delta G_{\text{PB}}) + 0.14852\Delta E_{\text{vdW}} + 0.05584\Delta G_{\text{SA}} + 0.11351(-T\Delta S) - 4.77148, \quad (6)$$

$$K_d = \ln \frac{\Delta G_{\text{bind}/\text{fitted}}}{RT}. \quad (7)$$

Here, ΔG_{bind} can be divided into three parts: the gas-phase molecular mechanics energy (ΔE_{MM}), the solvation free energy (ΔG_{sol}) and

the conformational entropy upon ligand binding ($T\Delta S$). ΔE_{MM} includes the electrostatic energy (ΔE_{ele}) and the van der Waals energy (ΔE_{vdW}). ΔG_{sol} is the sum of the polar contribution energy (ΔG_{PB}) and the nonpolar contribution energy (ΔG_{SA}). SASA represents the change in solvent-accessible surface area, γ is the surface tension coefficient, and b is a constant. γ and b were set as $2.27 \text{ kJ}\cdot\text{mol}^{-1}\cdot\text{nm}$ and $-23.85 \text{ kJ}\cdot\text{mol}^{-1}$, respectively. q_i and q_j are the charges of atom i and atom j in the protein, r_{ij} is the distance between atom i and atom j , ϵ_0 is the dielectric constant in vacuum, and ϵ_{in} is the relative dielectric constant. $\Delta G_{\text{bind}/\text{fitted}}$ was proposed [64] to fit binding free energy so that it can be consistent well with experimental results and K_d is the dissociation constant, where R is a constant with the value of $8.314 \text{ J}\cdot\text{mol}^{-1}\cdot\text{K}^{-1}$ and T is 310 K .

3. Results and discussion

3.1. MD simulations of $\alpha 7$ -apo/ $\alpha 7$ nAChR different ratio with CT16 complexes

We denote the resting state of $\alpha 7$ nAChR as $\alpha 7$ -apo, the complex with one bound CT16 as $\alpha 7\text{-}1$, and so forth, up to the complex with five bound CT16 ligands as $\alpha 7\text{-}5$, thereby constructing a total of six distinct systems. Subsequently, we conducted 100 ns simulations on the structures of $\alpha 7\text{-}i$ complexes. The simulations revealed that the overall structural integrity of all complexes was maintained. Fig. S1 illustrates the fluctuation behavior of Root-Mean-Square Deviation (RMSD) with increasing CT16 concentration. It can be observed that the six systems reached equilibrium within approximately 60 ns , and the RMSD values exhibited relatively stable fluctuations ($< 2 \text{ \AA}$) during the last 10 ns , indicating that all systems had achieved equilibrium so far. Additionally, previous studies have demonstrated that a simulation length of 100 ns is sufficient to effectively capture the key conformational dynamics in protein-protein systems of comparable scale [65–67]. Fig. S2 illustrates the fluctuation of the three replicate MD trajectories for the $\alpha 7\text{-}1/\alpha 7\text{-}3$, and the RMSD values exhibited relatively stable fluctuations ($< 2 \text{ \AA}$) during the last 10 ns , indicating that systems had also achieved equilibrium.

3.2. Locations of CT16 molecules on the $\alpha 7$ nAChR and induced allosteric effect of ECD

Fig. 2 illustrates the interaction domains of CT16- $\alpha 7$ nAChR complexes at distinct stoichiometric ratios (CT16: $\alpha 7$ nAChR = 1:1, 2:1, etc.). Docked results suggested that the first CT16 molecule binds at the interface between subunits D and E of the ECD region of $\alpha 7$ nAChR (Fig. 2(a1) and domain 1 in Fig. 2(g)), also the primary binding domain for other ligands, such as A β 42 and its short peptide fragments (A β 1–11, A β 1–16, A β 10–20, A β 12–28, A β 22–35) [18,68,69]. The spatial distribution of CT16 along the Y-axis extends from its C-terminal residue K16 to its N-terminal D1 (Fig. 2(f)), adopting a continuous and fully extended chain conformation (Fig. 2(a1)) to bind the receptor.

In $\alpha 7\text{-}1$, the residue E211 within the loop C of $\alpha 7$ nAChR interacts with D7 of CT16 through a hydrophobic network, while the residue K214 of loop C can form π -cation interactions with F4 and a hydrogen bond with E3 (Fig. 3(a1)). Both E211 and K214 are adjacent to the residue Y210, which is a key residue in the presynaptic modulation mediated by A β through aromatic side-chain interactions, located in the loop C region of subunit D [70–74]. These interactions result in a great decrease in the RMSF values in the loop C region of subunit D by 0.0334 nm , relative to that of $\alpha 7$ -apo, thereby enhancing the stability of this region (Fig. S3(d)).

In $\alpha 7\text{-}2$, the second CT16 is located in between subunits A and E (Figs. 2(b)(g)(b2)), becoming the neighbor of the first CT16 and in the similar orientation. Y210 and R208 within loop C on subunit E form hydrogen bonds and hydrophobic interactions with Y10 of CT16, respectively (Fig. 3(b2)), enhancing rather than the decreasing the dy-

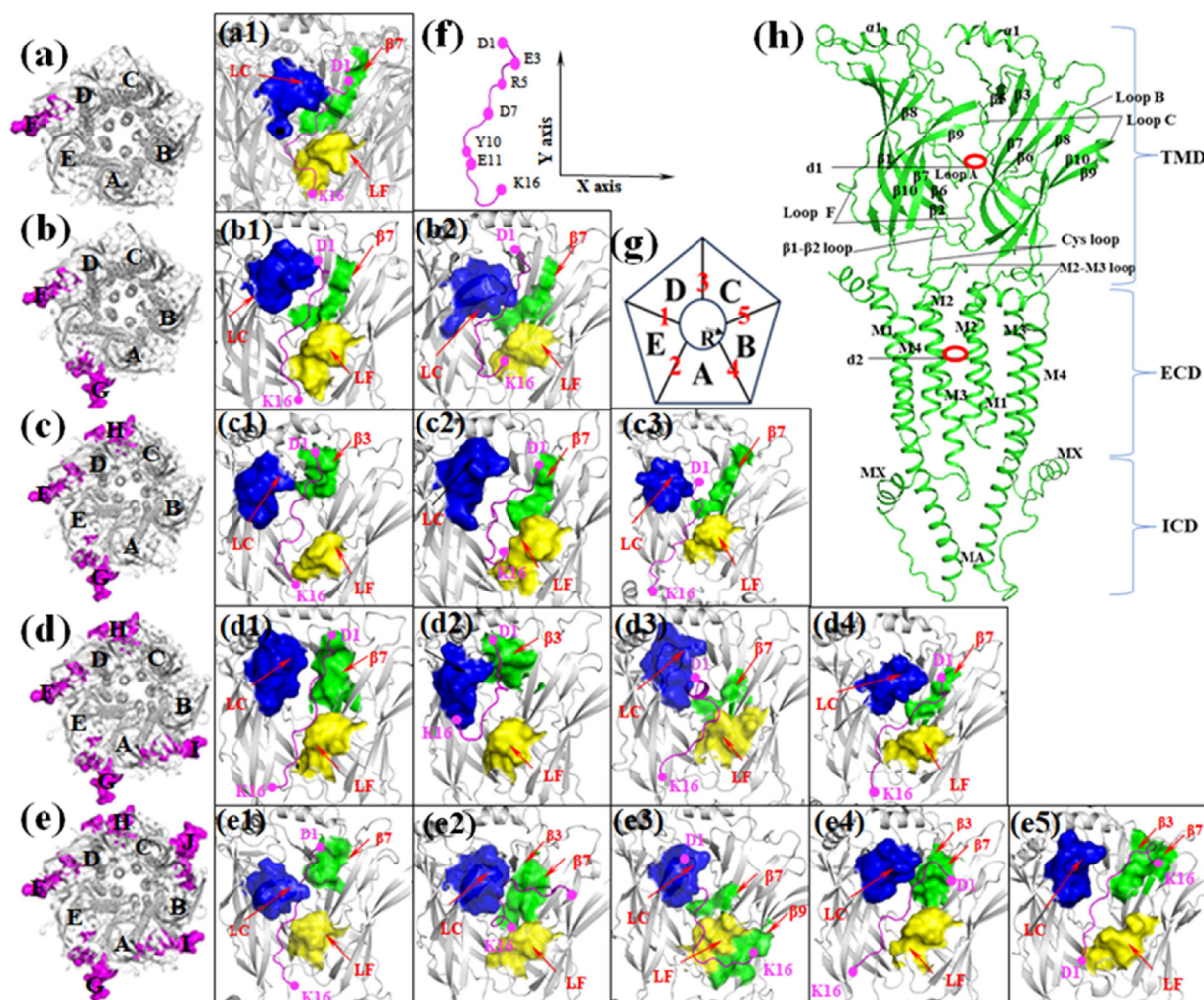


Fig. 2. Interaction domains of CT16 in $\alpha 7$ - i ($i = 1, 2, 3, 4,$ and 5) complexes. (a)–(e) represent the top views of $\alpha 7$ - i , in which the CT-16 is highlighted in magenta surface, and $\alpha 7$ nAChR receptor is displayed in grey. (a1)–(e5) depict the side views of the complexes $\alpha 7$ - i , in which i^{th} CT-16 bound is shown in pink with two terminal residues (D1 and K16) to mark the orientation of the CT16 peptide chain. ECD of $\alpha 7$ - i is shown in gray cartoon. Loops C and F, and β_j ($j = 3, 7,$ or 9) are displayed in blue and yellow, and green surfaces, respectively, to constitute the binding pockets. (f) Three-dimensional structure of CT16 and its charged residues in pink. (g) Pentameric skeleton drawing of $\alpha 7$ nAChR is displayed in (g) to define the specific site of i^{th} CT16 location, and the relative orientation of the five subunits, A, B, C, D, E. (h) Ribbon representation of two neighboring subunits of $\alpha 7$ nAChR, viewed parallel to the membrane plane, in which the secondary structural elements and loops are labeled. “LC” and “LF” in (a1)–(e5) stand for Loops C and F.

namics of loop C on subunit E (ΔRMSF at Y210 = + 0.031 nm) (Fig. S3(e)). Meanwhile, the binding of the first CT16 is impacted and altered (Figs. 2(b)(g)(b1)), and only a Y210-R5 hydrogen bond is observed (Fig. 3(b1)), recovering the loop C of subunit D to its initial state, i.e., in $\alpha 7$ -apo (Fig. S3(d)).

In $\alpha 7$ -3, the third CT16 binds between the loop C of subunit C and loop F of subunit D (Figs. 2(c)(g)(c3)), the clockwise neighbor of the first CT16 and in a similar orientation to the first and second CT16. K214 within loop C on subunit C form a salt bridge with E3 (Fig. 3(c3)), destabilizing the closed-state conformation and increasing flexibility of adjacent residues C213 (ΔRMSF = + 0.14 nm) and Y210 (ΔRMSF = + 0.21 nm) compared to that in $\alpha 7$ -apo (Fig. S3(c)). I191 within the loop F of subunit D forms a hydrophobic interaction with Y10, which also forms a hydrophobic interaction with Y151, reducing the RMSF value at this point by 0.014 nm compared to $\alpha 7$ -apo (Fig. S3(d)). Meanwhile, the binding case of the first CT16 also changes accordingly (Figs. 2(c)(g)(c1)). In addition to the observed originally Y210-D7 hydrogen bond (Fig. 3(c1)), a salt bridge is formed between R208 within the loop C of subunit D and E11 of the CT16, resulting in an increased flexibility of the loop C in subunit D (ΔRMSF at E211 = + 0.034 nm) (Fig. S3(d)). For the second CT16 (Figs. 2(c)(g)(c2)), the R208-E11 salt

bridge is still kept, while the previous R208-Y10 hydrophobic interaction and Y210-Y10 hydrogen bond disappear. Instead, Y10 participates in π -stacking and hydrophobic interactions with Y115 and W171 within subunit E, and hydrophobic interactions with W7 and P143 located in subunit A, and forms a hydrogen bond with L141 located in subunit A (Fig. 3(c2)). These residues form a cavity around Y10, tightly encircling it, increasing flexibility of adjacent residues G194 on loop F (ΔRMSF = + 0.13 nm) and C212 on loop C (ΔRMSF = + 0.20 nm) compared to the counterpart in $\alpha 7$ -2 (Fig. S3(e)), respectively, which contributes to the stabilization of the complex structure and enhancement of binding specificity [71–74].

In $\alpha 7$ -4, the fourth CT16 located between subunits A and B (Figs. 2(d)(g)(d4)), in the meta position of the first CT16 in the counterclockwise direction. Y210 within loop C on subunit A form hydrogen bonds with H6 of CT16 (Fig. 3(d4)), recovering the loop C of subunit A to its initial state, i.e., in $\alpha 7$ -apo (Fig. S3(a)). Meanwhile, the first CT16 changes its original conformation from its original bent state to a nearly linear one (Figs. 2(c)(g)(c1)), resulting in the distinction of the contacts of key residues. For example, compared to the counterparts in $\alpha 7$ -3, the salt bridge of R208-E11 (Fig. 3(d1)) is still kept, the hydrogen bond of Y210-D7 is lost however. Additionally, Y10 forms hydrophobic interac-

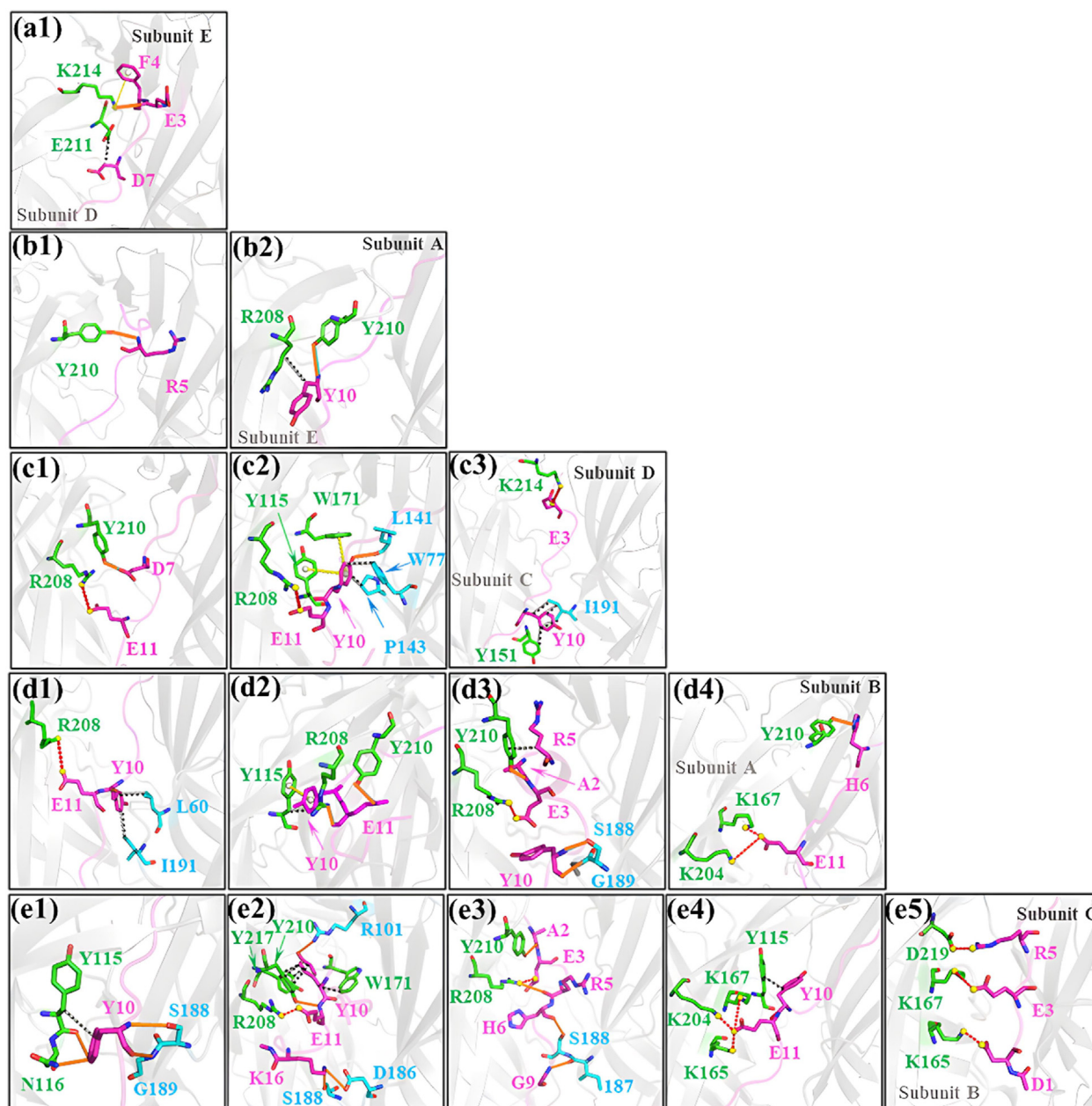


Fig. 3. Map of contact between ligand CT16 and key residues within loops C/F of two adjacent subunits of ECD in $\alpha 7$ -1 (a1), $\alpha 7$ -2 (b1)(b2), $\alpha 7$ -3 (c1)–(c3), $\alpha 7$ -4 (d1)–(d4) and $\alpha 7$ -5(e1)–(e5), respectively. The orange, black, red, and yellow dashes represent H bond (\AA), hydrophobic interaction, salt bridges, and π - π / π -cation interaction generated between CT16 and subunits. H-bond interactions were analyzed at a cutoff of 3.5 \AA for two heavy atoms. Five subunits of $\alpha 7$ - i ($i = 1, 2, 3, 4$, and 5) were represented in gray color, and ligand CT16 is represented in purple color. The residues within one subunit are colored in green, and the complementary residues within the other subunit are colored in cyan, respectively.

tions with I191 within the loop C of subunit E and L60 with the $\beta 1$ of subunit E (Fig. 3(d1)), enhancing the dynamics of loop C on subunit D (ΔRMSF at E211 = +0.23 nm) (Fig. S3(d)). Likewise, the second CT16 transforms into a mirror-image isomeric state (Figs. 2(d)(g)(d2)) compared to that in $\alpha 7$ -3 (Fig. 2(c2)). Correspondingly, the salt bridge of R208-E11 becomes a hydrogen bond connection, retaining only the π -stacking interaction between R208 and Y115. Y210-Y10 hydrogen bond (Fig. 3(d2)) decreases the dynamics of loop C on subunit D (ΔRMSF at C212 = -0.15 nm) (Fig. S3(e)). The binding of the third CT16 is also impacted and altered (Figs. 2(d)(g)(d3)). The region near N-terminal D1 of CT16 changes to an α -helix structure, resulting in the salt bridge between K214 and E3 disappears and a hydrogen bond and hydrophobic interaction produce between Y210 within loop C on subunit C and E3/A2 of CT16 (Fig. 3(d3)), decreasing the dynamics of loop C on sub-

unit C (ΔRMSF at C213 = -0.14 nm) (Fig. S3(c)). Simultaneously, S188 and G189 within loop F on subunit D form hydrogen bonds with Y10 of CT16 (Fig. 3(d3)), with the RMSF in the loop F region similar to the counterpart in $\alpha 7$ -2 (Fig. S3(c)).

In $\alpha 7$ -5, the fifth CT16 is located in between subunits B and C (Figs. 2(e)(g)(e5)), becoming the meta position of the first CT16 in the clockwise direction, exhibiting a reversed amino acid sequence orientation compared to the first four CT16 molecules, while maintaining an extended Y-axis alignment from N-terminal D1 to C-terminal K16 (Fig. 2(e5)). D219 within $\beta 10$, K165 and K167 within $\beta 7$ on subunit B form salt bridges interactions with R5, D1, and E3 of CT16, respectively (Fig. 3(e5)). The absence of direct residue interactions within loop C appears to confer enhanced dynamics to this region, as evidenced by the increased RMSF observed for subunit B at residue C212

Table 1
Binding free energies (kcal mol⁻¹) of complexes using MM/PBSA.

Name	ΔE_{PB}	ΔE_{SA}	ΔE_{COU}	ΔE_{vdW}	$T\Delta S$	ΔG	$\Delta G_{\text{bind/fittd}}$
$\alpha 7-1-1$	270.93	-14.02	-193.39	-89.36	38.97	13.13	-10.21
$\alpha 7-2-1$	200.62	-13.37	-140.55	-80.74	36.74	2.70	-10.09
$\alpha 7-2-2$	142.07	-14.06	-59.14	-103.73	27.89	-6.97	-13.32
$\alpha 7-3-1$	177.97	-11.08	-126.67	-61.95	29.57	7.85	-8.46
$\alpha 7-3-2$	117.33	-11.01	-68.59	-69.62	31.69	-0.21	-9.50
$\alpha 7-3-3$	226.86	-13.04	-154.25	-74.57	42.20	27.21	-7.86
$\alpha 7-4-1$	208.71	-14.24	-122.81	-87.37	27.19	11.49	-10.82
$\alpha 7-4-2$	162.95	-11.02	-95.34	-63.74	32.41	25.26	-7.52
$\alpha 7-4-3$	233.62	-12.31	-163.31	-72.88	17.17	2.29	-10.54
$\alpha 7-4-4$	263.94	-12.34	-177.46	-65.31	27.49	36.33	-7.37
$\alpha 7-5-1$	165.10	-13.94	-82.43	-92.45	16.89	-6.83	-12.90
$\alpha 7-5-2$	104.37	-10.23	-45.71	-63.93	30.97	15.47	-8.15
$\alpha 7-5-3$	238.56	-12.98	-146.34	-93.58	21.50	7.16	-11.97
$\alpha 7-5-4$	262.86	-13.42	-169.73	-71.21	20.90	29.41	-8.69
$\alpha 7-5-5$	156.23	-13.00	-84.91	-79.12	35.20	14.40	-9.40

($\Delta\text{RMSF} = +0.15$ nm) (Fig. S3(b)). Notably, this binding event also induces allosteric rearrangements for pre-bound four CT16 molecules. For the first CT16, only two N116-Y10 hydrogen bonds and one Y115-Y10 a hydrophobic interaction is observed (Fig. 3(e1)), decreasing flexibility of adjacent residues E211 on loop C ($\Delta\text{RMSF} = -0.063$ nm) within subunit D compared to that in $\alpha 7-4$ (Fig. S3(d)). For the second CT16, it changes from an original distribution along the Y-axis to the X-axis, and transitions from an extended to a crescent shape, a notable change in contact means. Especially, R208, a positively charged residue located in Loop C of subunit E, forms a salt bridge with negatively charged E11 of CT16, as opposed to a hydrogen bond observed in $\alpha 7-4$, resulting in enhanced Loop C dynamics (ΔRMSF at E211 = +0.057 nm, Fig. S3(e)). For the third CT16, it adopts a mirror-image enantiomer of the third CT16 of $\alpha 7-4$ (Fig. 2(d3)), with several key changes observed. R208 of subunit C forms a salt bridge with E3 and a hydrogen bond with R5 of CT16, relieving the hydrophobic interaction of A2 with Y210 (Fig. 3(e3)), reverting Loop C in subunit C to a conformation like that within $\alpha 7-4$ (Fig. S3(c)). Meanwhile, the dynamics of Loop F within subunit D are reduced, as S188 and I187 form hydrogen bonds with G9 of CT16, reducing the ΔRMSF at D186 by -0.055 nm (Fig. S3(d)). For the fourth CT16 binding, the binding pattern largely remains consistent with that in $\alpha 7-4$ (Fig. 2(e4)). Notably, K165 forms a salt bridge with E11, and Y115 engages in a hydrophobic interaction with Y10 (Fig. 3(e4)). The absence of interactions between Loop C and CT16 in this context leads to increased Loop C dynamics in subunit B (ΔRMSF at C212 = +0.06 nm, Fig. S3(a)).

3.3. Binding free energy between $\alpha 7\text{nAChR}$ and CT16 in $\alpha 7-i$ complexes

ΔG_{bind} is decomposed into five terms, ΔE_{vdW} , ΔE_{COU} , ΔG_{PB} , ΔG_{SA} , and $-T\Delta S$. These ΔG_{bind} values in Table 1 of the 15 systems are all negative, indicating strong binding between CT16 and $\alpha 7\text{nAChR}$. To clarify the binding energy for specific CT16 molecule, these $\alpha 7-i$ complexes are renamed as $\alpha 7-i-j$, where ‘j’ indicates the ordinal position of the bound CT16 molecule and the binding energy calculated is also just for it. For example, $\alpha 7-2-1$ and $\alpha 7-2-2$ in Table 1 stand for the binding energies of first and second CT16 respective to the remaining complex $\alpha 7-1$ part of the $\alpha 7-2$ complex. The dissociation constant $K_{\text{d}} = 9.0$ μM was measured in the experiment [75] for $\alpha 7\text{nAChR-A}\beta 1-42$ interaction, just corresponding to binding energy of -12.10 kcal·mol⁻¹, converted by Eq. (7) in the Section 2.3. The value is less than that (-13.32, vs -12.90 kcal·mol⁻¹) of $\alpha 7-2-2$ and $\alpha 7-5-1$, larger than others of $\alpha 7-i-j$ complexes predicted in the present paper (see details in Table 1).

This study demonstrates that the interaction between CT16 ligands and $\alpha 7\text{nAChR}$ is significantly influenced by a site-specific energy-driven pattern. In the contribution of binding energy, electrostatic interactions and van der Waals forces play predominant roles. For example, electrostatic interactions in the $\alpha 7-1-1$ site reaches $\Delta E_{\text{COU}} = -193.39$

kcal·mol⁻¹, accounting for 68% of the total contribution, indicating a dominant contribution to the initial ligand binding. This is primarily due to the complementary interactions between charged residues at the subunit interface, such as the salt bridge formed between K214 and the ligand E3 at the D-E interface (Fig. 3(a1)). Van der Waals forces, on the other hand, facilitate subsequent ligand binding, as in the $\alpha 7-2-2$ site, where ΔE_{vdW} (-103.73 kcal·mol⁻¹) constitutes 64% of the total energy. This promotes stable binding through the formation of hydrophobic cavities, such as the π - π stacking between Y210 and Y10 at the A-E interface (Fig. 3(b2)). Notably, the third ligand site ($\alpha 7-3-3$) exhibits electrostatic dominance again (ΔE_{COU} accounting for 67%), due to the reformation of the salt bridge between K214 and E3 (Fig. 3(b3)). This indicates that allostery can reshape the pattern of energy contribution. This finding further elucidates how $\alpha 7\text{nAChR}$ achieves multi-ligand cooperative binding through dynamic adjustment of different types of interaction forces. Additionally, the impact of the sequential nature of ligand binding on binding strength reveals a non-linear regulatory characteristic (Figs. 2(g) and 5). The second ligand ($\alpha 7-2-2$) forms a peak in binding energy ($\Delta G = -13.32$ kcal·mol⁻¹), primarily benefiting from its spatial coupling effect with the first ligand (adjacent D-E and A-E interfaces inducing cooperative binding). The binding of the fifth ligand triggers a global conformational rearrangement (Fig. 2(e5)), resulting in a 32% reduction in the van der Waals interaction of the first ligand ($\Delta E_{\text{vdW}} = -92.45$ kcal·mol⁻¹ for $\alpha 7-5-1$ compared to -89.36 kcal·mol⁻¹ for $\alpha 7-1-1$), revealing the presence of negative cooperativity.

Ultimately, the spatial differences in binding sites determine the ligand binding affinity (Fig. 2(g)). High-affinity sites are primarily located at the subunit interface regions, including the D-E interface (first ligand site, $\Delta G = -10.21$ kcal·mol⁻¹) and the A-E interface (second ligand site, $\Delta G = -13.32$ kcal·mol⁻¹), which exhibit both electrostatic complementarity and hydrophobic cavities, thereby supporting strong binding interactions. In contrast, low-affinity sites are distributed in the monomer core region, where the A-B interface ($\alpha 7-4-4$, $\Delta G = -7.37$ kcal·mol⁻¹) and the B-C interface ($\alpha 7-5-5$, $\Delta G = -9.40$ kcal·mol⁻¹) have a contribution of van der Waals interactions of <50% due to steric hindrance.

3.4. Analysis of PCA and FEL

To further evaluate the conformational dynamics of $\alpha 7\text{nAChR}$ under different ligand-bound states, we performed principal component analysis (PCA) on the MD trajectories. The first two principal components (PC1 and PC2), which together accounted for >70% of the total variance, were used to construct the free energy landscapes (FELs). As shown in Fig. 4, the ligand-free $\alpha 7\text{nAChR}$ (Fig. 4(a)) displays a broad and diverse conformational ensemble with multiple local minima scattered across the PC1-PC2 space, suggesting substantial conformational

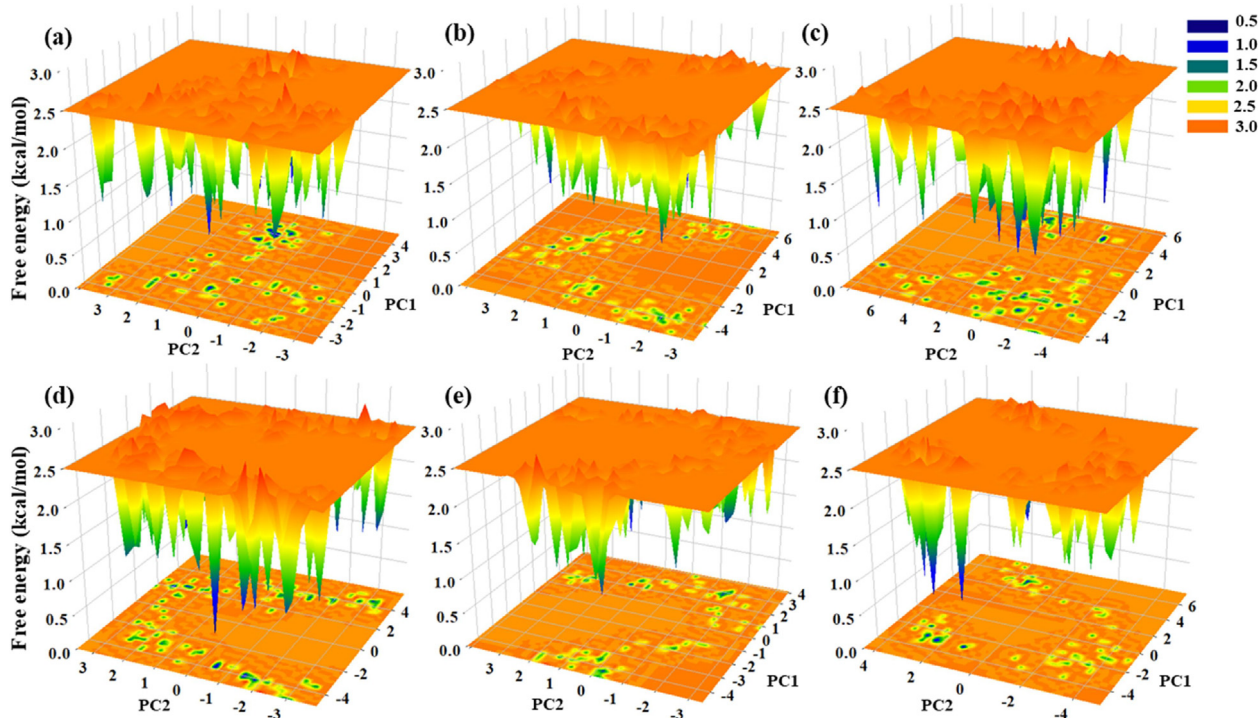


Fig. 4. 3D/2D free energy landscapes of the $\alpha 7$ nAChR conformation in $\alpha 7$ -apo (a), $\alpha 7$ -1 (b), $\alpha 7$ -2 (c), $\alpha 7$ -3 (d), $\alpha 7$ -4 (e) and $\alpha 7$ -5 (f), respectively. PC1 and PC2 are the two largest eigenvectors. Color bars in orange and black represent the conformational space with maximum energy (conformational instability) and minimum energy (conformational stability), respectively.

plasticity. Upon increasing ligand occupancy (Figs. 4(b)–(f)), the free energy minima become progressively deeper and more localized, indicating a reduction in conformational entropy and a tendency toward specific metastable states.

Notably, the three to five ligand bound systems (Figs. 4(d)–(f)) exhibit a clear convergence to a dominant low-energy basin, implying that ligand binding imposes structural constraints that stabilize specific gating-related conformations. Furthermore, comparative analysis of the dominant PC vectors revealed that PC1 primarily represents a collective twisting motion of the ECD, while PC2 reflects an inward-outward breathing of the ICD (see details in Fig. 8).

Overall, these PCA-FEL results provide mechanistic insight into how increasing ligand concentration modulates the dynamic landscape of $\alpha 7$ nAChR, restricting its flexibility and favoring the transition into functionally relevant conformational substates.

3.5. Pore radius changes in $\alpha 7$ -apo/ $\alpha 7$ -i complexes

To further estimate pore diameters structural visualization and figure preparation, we performed pore radius for $\alpha 7$ -apo/ $\alpha 7$ -i ($i = 1, 2, 3, 4$, and 5) using the Hole website [57] and software packages Chimera [58], and then showed the results in Fig. 5. Within these $\alpha 7$ -apo/ $\alpha 7$ -i complexes, the pore diameter varies as the ion permeates from the ECD, TMD, to ICD regions. Across the whole ion channel, the pore radius changes along with both the pore sites (goes down from ECD to ICD) and the number of bound CT16 (Fig. 7). Notably, in the ECD region, there are two notable chambers observed in $\alpha 7$ -2 and $\alpha 7$ -3, (Figs. 5(c)(d)), and one chambers observed in $\alpha 7$ -apo, $\alpha 7$ -1, $\alpha 7$ -4, and $\alpha 7$ -5 (Figs. 5(a)(b)(e)(f)), which are associated closely to the number of CT16 bindings and poses of CT16 binding with the Loops C/F. Correspondingly, two narrowest pore diameters (d1 and d2, in Fig. 5) reported experimentally [71–74], are also observed at the sites of residues E120 and L270, respectively (Figs. 5,6). As the two narrowest pores, especially the d2 pore, were identified as the key channel gating for ion permeability

[19], both d1 and d2 will be discussed in detail for their changes as the ratio of CT16 increase.

Despite the experimental confirmation that diameter d2 (L270) is narrower than d1 and identified as the primary determinant for the passage of a hydrated cation [21], present result reveals that things are not always the case, dependent on the ligand species, concentration and so on. In $\alpha 7$ -1, d1 ($1.31 \times 2 \text{ \AA}$) (Figs. 6(a)(b)) is smaller than d2 ($1.51 \times 2 \text{ \AA}$) (Figs. 6(a)(c)) but larger than d1 of $\alpha 7$ -apo. Furthermore, d2 of $\alpha 7$ -1 is also larger than that of $\alpha 7$ -apo, indicating that one CT16 does enable to activate the $\alpha 7$ -apo and the residue E120 in the ECD rather than L270 within TMD is the primary determinant for ion permeability. This finding is consistent with the conclusion that ACh can activate the $\alpha 7$ nAChR by occupying just one neurotransmitter-binding site [26], which are sufficient to destabilize the closed state and stabilize the open state. Unfortunately, which residue is the primary determinant for the ion permeability remain unknown so far in the presence of ligand ACh. Although experimental data lack conclusive evidence that the E120 residue directly governs molecular size selection in the $\alpha 7$ nAChR channel, they suggest this evolutionarily conserved residue plays a structural and functional role in modulating the ion permeation pathway [19], indicating that d1 does be possible to the primary determinant for ion permeability in some case.

The pore radius at residue L270 (d2) of $\alpha 7$ -apo measured as only 1.30 \AA (see the bottom of Fig. 5(a) and Fig. 6(c)), with a pore diameter of 2.60 nm , are consistent well with two experimental results (2.8 \AA [21] and 2.4 \AA [19]), indicating a closed channel state [21] and the reliability of the present predication. When ligand CT16 ratio increases from 1 to 5, the diameters d2 grows up from $3.02, 3.04, 3.22, 3.10$, and 2.88 \AA , respectively, with the maximum of 3.22 \AA in $\alpha 7$ -3, and minimum 2.88 \AA in $\alpha 7$ -5 (larger than 2.6 \AA in $\alpha 7$ -apo), indicating the channel is activated and potential multifunctional modifier, when the CT16 ligand with multi-ratio is bound. The activated effect is different from ACh, which was once identified that 1:1 ratio of ACh: $\alpha 7$ nAChR is sufficient for the channel activation and increased concentration of ACh will hardly produce a maximal response [26].



Fig. 5. Permeation pathway depicting hydrophobicity and pore diameter of (a) $\alpha 7$ -apo, (b) $\alpha 7$ -1, (c) $\alpha 7$ -2, (d) $\alpha 7$ -3, (e) $\alpha 7$ -4, and (f) $\alpha 7$ -5. Top panel: Two/three chambers are highlighted in red or orange, which are wrapped in ECD and ICD regions. Two regions with the narrowest pore diameter are marked in red and black lines, corresponding to the sites of residues E120 (d1) of ECD region and L270 (d2) within TMD region, respectively. Bottom panel: two M2 helices of the TMD region are selected to characterize their conformation and clarify the site of residue L270 and corresponding pore diameters (\AA), in line with the points of interest indicated by black dashed lines in top panel.

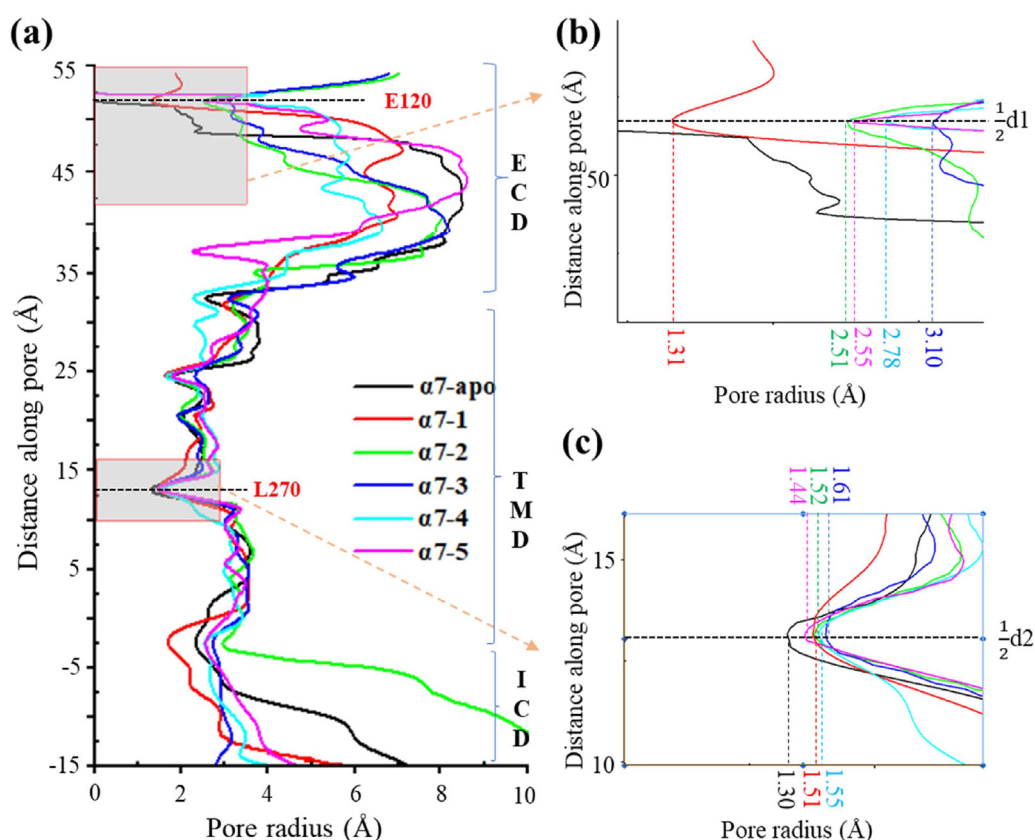


Fig. 6. (a) The pore profile traces comparing $\alpha 7$ -apo/ $\alpha 7$ different ratio with CT16 state structure. (b) Aperture magnification at E120; (c) Aperture magnification at L270.

Of particular note is that these activated diameters are all far less than the actual ones observed experimentally. For example, 10 \AA and 7.2 \AA diameters were determined by Zhao et al. [21] and Noviello et al. [19], respectively, in which different ligands, EVP-6124 and agonist epibatidine α -bgt, in combination with similar positive allosteric modulator PNU are, respectively, employed. Zhao et al. [21] investigated

an increase in the diameter of the transmembrane pore near L270 to approximately 10 \AA in EVP-6124/PNU-bound $\alpha 7$ nAChR, which is approximately 2.8 \AA larger than the pore diameter mentioned previously. Therefore, the larger difference in the activated diameter not only derived from the different ligand bound but also the presence or absence of positive allosteric modulator, as it enables to enhance the likelihood

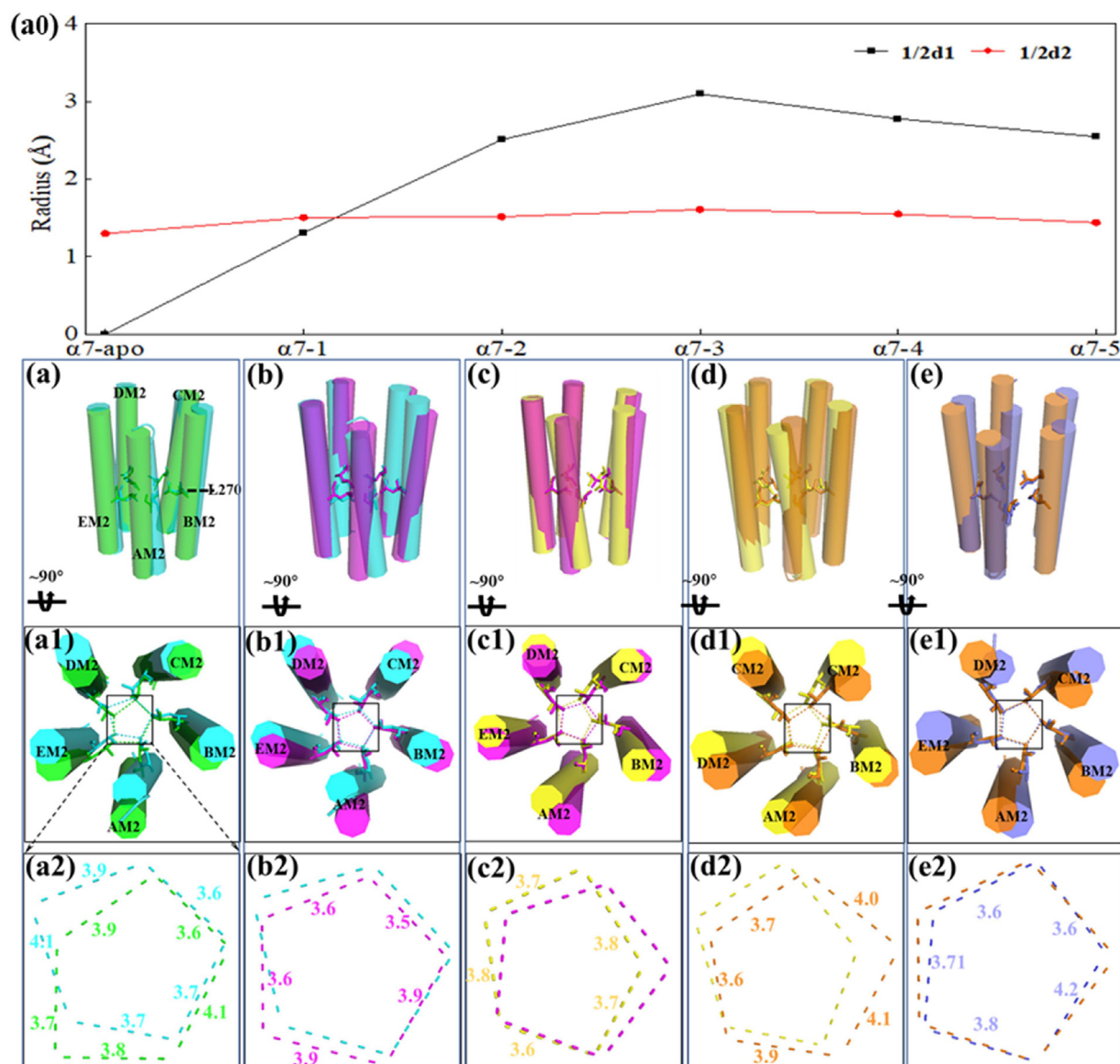


Fig. 7. (a0) The radius correspondence of the narrowest pores (1/2d1 vs 1/2d2) in the regions of ECD and TMD, as the CT16 ratio increases in $\alpha 7$ -apo/ $\alpha 7$ - i ($i = 1, 2, 3, 4,$ and 5). (a)–(e) Side views of the pore lining M2 helices of TMD are shown for pairs of $\alpha 7$ -apo (green) and $\alpha 7$ -1 (blue) (a), of $\alpha 7$ -1 and $\alpha 7$ -2 (magenta) (b), of $\alpha 7$ -2 and $\alpha 7$ -3 (yellow) (c), of $\alpha 7$ -3 and $\alpha 7$ -4 (orange) (d), of $\alpha 7$ -4 and $\alpha 7$ -5 (light blue) (e), in which the hydrophobic gated residues of L270 in the five subunits are shown as sticks. (a1)–(e1) Top-down views of the pore lining M2 helices of TMD, where the L270 residues can be confronted to highlight the conformational changes within the channel pore. The distance between five adjacent residues of L270 in the $\alpha 7$ -apo/ $\alpha 7$ - i ($i = 1, 2, 3, 4,$ and 5) structure. (a2)–(e2) The changes are displayed and compared for the side length in pentagons formed by connecting the innermost heavy atoms of the five residues L270 across the five subunits, so that an allosteric mechanism can be proposed from the symmetric shift of pentagon as the CT16 ratio increases.

of agonist-induced channel activation, prolong open-channel durations, and mitigate desensitization phenomena. Therefore, the addition of a positive allosteric modulator is necessary [21]. Nonetheless, our results (without a positive allosteric modulator employed) still provide insights into the influence of concentration changes of CT16 on the receptor $\alpha 7$ nAChR.

Additionally, our result reveals that binding of one to five CT16 molecules can activate $\alpha 7$ nAChR, with the pore diameter initially increasing and then decreasing as the number of ligands increases, reaching maximum activation with three CT16 molecules bound. This finding is consistent with the conclusion that ACh can activate the $\alpha 7$ nAChR by occupying just one neurotransmitter-binding site [26]. However, it differs somewhat from the conclusion that low concentrations of $A\beta$ (picomolar) can activate $\alpha 7$ nAChR, while high concentrations inhibit it [39,76].

The distinction derive from the supersaturated $A\beta$ reactants in the actual experimental operation, no matter the low concentrations or higher concentrations of $A\beta$ –1–16/CT16 defined for the interaction of CT16- $\alpha 7$ nAChR, suggesting that $A\beta$ 1–16 can activate $\alpha 7$ nAChR at low concentrations (pM–nM) [40,76], while it exhibits inhibitory effects at higher concentrations (μ M–mM) [39]. For example, in the experiment conducted by Matfíaset al. [39], $A\beta$ 1–42 at concentrations of 0.1 nM and 100 nM was incubated with Torpedo membranes or BOSC-23 cells expressing $\alpha 7$ nAChR at a protein concentration of 100 μ g/mL, resulting in a molar ratio close to 15:1. Therefore, the concentration-dependent bidirectional regulation of $A\beta$ observed experimentally is primarily attributed to the dynamic interplay between $A\beta$ supramolecular assembly states (rather than individual monomers) and $\alpha 7$ nAChR conformational plasticity [77–79] a mechanism which exceeds the explanatory scope of current stoichiometric modeling approaches.

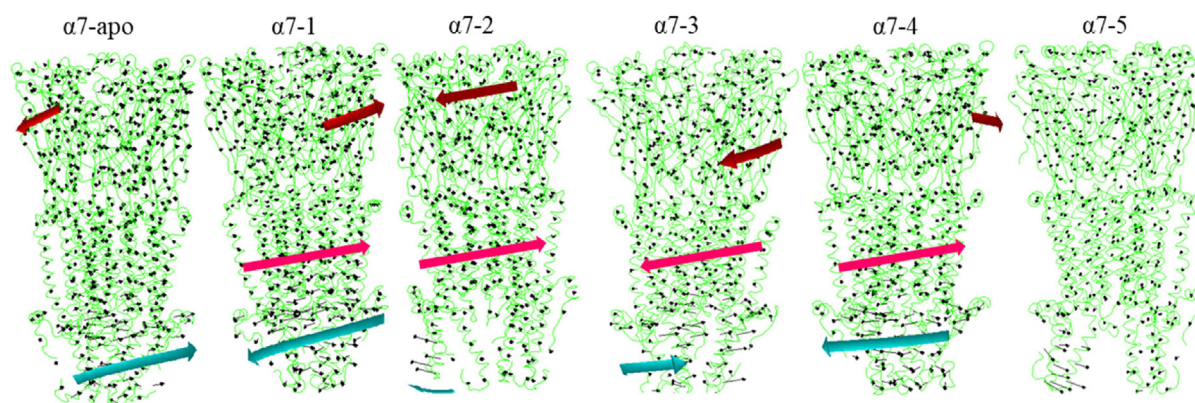


Fig. 8. Dynamical network analysis of the $\alpha 7$ -apo/ $\alpha 7$ - i ($i = 1, 2, 3, 4,$ and 5). Vector arrows in dark red, red and green stands for the twist orientation and strength (arrow length) of the ECD, TMD and ICD regions, respectively.

3.6. Structure-activity relationship of influencing pore size distribution

How CT16 concentration gradients orchestrate inter-domain allosteric networks to achieve bidirectional ECD-TMD conformational synchronization during gating transitions remains a fundamental unresolved question. The presence of CT16 with different ratio can trigger the conformational changes of the ECD region directly, as dissected in Section 3.2. The outcome of the conformational changes is associated closely to the changes of the narrowest pore diameter (d_1) in the region, and as a result of the d_2 in the TMD region. The association of d_1 and d_2 is displayed in Fig. 7(a0) by summarizing the data presented in Figs. 5,6. The result shows that d_1 changes within ECD are positively related with, but not a linear correlation with the d_2 changes in the TMD. Both d_1 and d_2 results in $\alpha 7$ - i are larger than the counterparts of $\alpha 7$ -apo, suggesting that both narrowest pores are activated in the presence of the CT16 with ratio of 1–5. More notably, the pore size (d_1) in the ECD domain increases very rapidly with the increase of CT16 concentration, much faster than the pore size in the TMD domain. This may be related to the direct interaction between the ECD domain and CT16. Clearly, the change in pore size (d_2) in the TMD domain is caused by conformational changes transmitted by the binding of CT16 in the ECD domain. Although the change in pore size in the TMD domain is not as significant as that in the ECD domain, it still shows a consistent pattern with the change in pore size in the ECD domain as the CT16 concentration varies.

Therefore, we propose that CT16 binding to the ECD domain induces conformational changes in the TMD domain, consequently modulating the pore size. For detailed mechanistic insights, we constructed pentagons by connecting the innermost heavy atoms (CD2) of the five residues L270 across the five subunits (Figs. 7(a1)–(e1)) in the TMD region (Figs. 6(a)–(e), top view). Figs. 7(a2)–(e2) displays the side lengths of the five pentagons of $\alpha 7$ -apo/ $\alpha 7$ - i , in which pairs of $\alpha 7$ -apo and $\alpha 7$ -1, of $\alpha 7$ -1 and $\alpha 7$ -2, ..., of $\alpha 7$ -4 and $\alpha 7$ -5 are overlapped and compared with each other, respectively. For $\alpha 7$ -apo/ $\alpha 7$ - i systems, the corresponding side lengths in the Figs. 7(a2)–(e2) were employed to calculate standard deviation (SD). SD is widely employed to evaluate the regularity of geometric shapes (e.g., consistency in polygon side lengths) as it directly quantifies data variability [80]. In the analysis of regular polygons, an SD of 0 represents the ideal state, and values closer to 0 indicate higher regularity. The SD was calculated using the formula of SD

$$= \sqrt{\left[\frac{1}{N} \sum_{i=1}^N (x_i - \mu)^2 \right]}$$

where μ denotes the mean value, x_i represents individual side length measurements, and N is the number of data points (here, $N = 5$). The resultant SD values in $\alpha 7$ - i were 0.172, 0.178, 0.167, 0.075, 0.185, and 0.223 respectively, when $i = 1, 2, 3, 4,$ and 5 . Notably, the SD values progressively decreased from $\alpha 7$ -1 to $\alpha 7$ -3 (reaching minimum), followed by a gradual increase. This dynamic trajectory

suggests that CT16 binding triggers a reversible symmetry shift within the TMD, progressing through an intermediate symmetric state before re-establishing structural asymmetry. These findings align with previous reports by Mackenzie et al. [81], demonstrating that agonist binding triggers global ECD movements, facilitating conformational transitions from asymmetric to symmetric states during channel opening.

To further validate this symmetry transition and characterize global conformational fluctuations, we performed dynamical network analysis (DNA) [82] for $\alpha 7$ -apo/ $\alpha 7$ - i ($i = 1, 2, 3, 4,$ and 5) using the iMODS [83–85] website, and shown the results in Fig. 8. With the increase in the number of ligands bound, the $\alpha 7$ nAChR receptor exhibits significant conformational dynamics. In $\alpha 7$ -apo, the ECD undergoes an inward deflection, while ICD undergo a coordinated outward expansion, indicating a tightened rotation of the conformation through the TMD. Interestingly, the rotation orientation is opposite to that of the helix bundles in the TMD. Upon binding a single ligand ($\alpha 7$ -1), The vector arrows in $\alpha 7$ -1 become longer than that in $\alpha 7$ -apo in combination with an increased twist from the TMD (see red arrow in Fig. 8 $\alpha 7$ -1), indicating a more tightened rotation of the receptor conformation, but a more open state of the pore formed by the M2/M3 helices in the TMD due to the pulling effect of ligand binding on the local ECD structure. In the presence of two ligands ($\alpha 7$ -2), the deflection of the ECD region is significantly enhanced, with the C-loop further retracting towards the receptor's center, the opposite deflection of the TMD region along with attenuated offset from the deflection of the ICD drive the continuous increase in the M2/M3 helix spacing in the TMD region, indicating an increased probability of channel opening. When the number of ligands increases to three ($\alpha 7$ -3), the two reverse vector arrows from respective ECD and ICD become shorter, and almost equivalent to each other, indicating a gentle twist of the TMD only derive from the itself domain, favoring the helix expansion in the TMD region, and resulting in a maximum open conformation for efficient ion permeation.

Notably, at higher ligand loading states ($\alpha 7$ -4/ $\alpha 7$ -5), the conformational adjustment of the ECD tends to stabilize. In $\alpha 7$ -4, the degree of C-loop inward movement diminishes while the twists in both TMD and ICD remains highly and almost equally but reversely expanded, indicating a restrained open of the ion channel, relative to that in $\alpha 7$ -3; in $\alpha 7$ -5, there is a stagnation in ECD deflection and a plateau in TMD expansion, suggesting that the receptor becomes locked in a stable state upon saturation with ligands. Therefore, the DNA reveals a CT16-concentration dependent ECD-TMD-ICD allostery coupling mechanism, realizing the entire process of gate transition from initial activation (single ligand), progressive opening (dual ligands), complete conductance (triple ligands), to steady-state maintenance (four to five ligands), providing a molecular conformational basis for understanding the ligand concentration-dependent activation mechanism of the $\alpha 7$ nAChR receptor.

3.7. Comparing the binding effects of the monomer and dimer with the $\alpha 7nAChR$

To address potential dimerization effects at high CT16 concentrations, we simulated the binding of two CT16 monomers. Results show pore dilation at L270 site in the dimeric complex ($\alpha 7-11$) increases to 3.10 Å (Fig. S4(c)), becoming larger than that of 3.02 Å in $\alpha 7-1$ and 2.60 Å in $\alpha 7$ -apo, respectively. Therefore, high concentrations of CT16 indicate not only multi-site binding preference of the ligand but also possible local single-site binding. Regarding the dimer binding under current investigation, it promotes pore opening more effectively than monomer binding, thus enhancing ion transport through channels.

4. Conclusions

This study provides a detailed molecular dynamics simulation analysis of the concentration-dependent effects of CT16 on the $\alpha 7nAChR$. Our findings demonstrate that CT16 binds to the $\alpha 7nAChR$ at its ECD region in a particular sequence and specific patterns, inducing conformational changes that affect the receptor's structural integrity and ion permeability.

The present result predicted for the first time that the narrowest pore (d1) in the ECD would be the major determinant for the ion permeation when the $\alpha 7nAChR$:CT16 stoichiometry is low at 1:1. From 1:1 to 1:5, the narrowest pores in both the ECD and TMD are larger than the counterparts in $\alpha 7$ -apo, of indicative of the activated effect of these different CT16 ratios, and the pore in TMD (d2) become the major determinant for the ion permeation, aligning well with the experimental observations [19,21].

MD simulations demonstrated that CT16 binding progressively reshapes receptor symmetry and pore geometry. Intermediate occupancy (3 ligands) maximizes pore dilation (3.22 Å), whereas high occupancy (5 ligands) induces near-complete closure (2.88 Å), which clearly define the relationships of structure-function, as well as the CT16 dose effect. These results highlight the potential of CT16 as both a modulator of $\alpha 7nAChR$ function and a therapeutic target for AD and related neurodegenerative disorders, revealing a triphasic activation-inhibition mechanism governed by ligand stoichiometry. Mechanically, the modulation effect of different CT16 ratios on pore alteration depends on the degree of receptor symmetry impairment and restoration caused by the number of ligands, in which opposite twist of the ECD and ICD is the potential regulator.

This study acknowledges certain limitations, primarily the insufficient consideration of the influences of positive allosteric modulators and membrane environmental factors on the outcomes, which may have contributed to substantial discrepancies between the simulated results and actual experimental data. Nonetheless, the simulation analysis revealed trends that were consistent with the experimental observations, thereby substantiating the critical role of CT16 concentration in the regulatory process. Future research endeavors will aim to refine the model by incorporating a broader range of influencing factors to enhance the predictive accuracy.

Declaration of Competing Interest

The authors declare that they have no known competing financial interests or personal relationships that could have appeared to influence the work reported in this paper.

CRedit authorship contribution statement

Chuanbo Wang: Writing – original draft, Visualization, Validation, Methodology, Investigation, Formal analysis, Data curation, Conceptualization. **Jinfei Mei:** Investigation, Formal analysis. **Mengke Jia:** Validation, Methodology, Investigation, Formal analysis. **Sajjad Ahmad:**

Validation. **Zijian Liu:** Validation. **Hongqi Ai:** Writing – review & editing, Supervision, Resources, Project administration, Funding acquisition, Conceptualization.

Acknowledgements

This work was supported by the Shandong Provincial Natural Science Foundation (ZR2022MB073) of China.

Supplementary materials

Supplementary material associated with this article can be found, in the online version, at doi:10.1016/j.chphma.2025.07.001.

References

- [1] K.N. Hascup, C.A. Findley, J. Britz, N. Esperant-Hilaire, S.O. Broderick, K. Delfino, S. Tischkau, A. Bartke, E.R. Hascup, Riluzole attenuates glutamatergic tone and cognitive decline in *A β PP/PS1* mice, *J. Neurochem.* 156 (2021) 513–523, doi:10.1111/jnc.15224.
- [2] D.J. Selkoe, Alzheimer's disease is a synaptic failure, *Science* 298 (2002) 789–791, doi:10.1126/science.1074069.
- [3] D.A. Gusnard, M.E. Raichle, Searching for a baseline: Functional imaging and the resting human brain, *Nat. Rev. Neurosci.* 2 (2001) 685–694, doi:10.1038/35094500.
- [4] M. Sastre, H. Steiner, K. Fuchs, A. Capell, G. Multhaup, M.M. Condron, D.B. Teplow, C. Haass, Presenilin-dependent γ -secretase processing of β -amyloid precursor protein at a site corresponding to the S3 cleavage of Notch, *EMBO Rep.* 2 (2001) 835–841, doi:10.1093/embo-reports/kve180.
- [5] A. Weidemann, S. Eggert, F.B.M. Reinhard, M. Vogel, K. Paliga, G. Baier, C.L. Masters, K. Beyreuther, G. Evin, A novel ϵ -cleavage within the transmembrane domain of the Alzheimer amyloid precursor protein demonstrates homology with Notch processing, *Biochemistry* 41 (2002) 2825–2835, doi:10.1021/bi015794o.
- [6] C. Haass, C. Kaether, G. Thinakaran, S. Sisodia, Trafficking and proteolytic processing of APP, *Cold Spring Harb. Perspect. Med.* 2 (2012) a006270, doi:10.1101/csh-perspect.a006270.
- [7] S. Ludewig, M. Korte, Novel insights into the physiological function of the APP (gene) family and its proteolytic fragments in synaptic plasticity, *Front. Mol. Neurosci.* 9 (2017) 161, doi:10.3389/fnmol.2016.00161.
- [8] D. Kögel, T. Deller, C. Behl, Roles of amyloid precursor protein family members in neuroprotection, stress signaling and aging, *Exp. Brain Res.* 217 (2012) 471–479, doi:10.1007/s00221-011-2932-4.
- [9] H.C. Rice, D. de Malmazet, A. Schreurs, S. Frere, I. Van Molle, A.N. Volkov, E. Creemers, I. Vertkin, J. Nys, F.M. Ranaivoson, D. Comoletti, J.N. Savas, H. Remaut, D. Balschun, K.D. Wierda, I. Slutsky, K. Farrow, B. De Strooper, J. de Wit, Secreted amyloid- β precursor protein functions as a GABA_BR1a ligand to modulate synaptic transmission, *Science* 363 (2019) aao4827, doi:10.1126/science.aao4827.
- [10] M.C. Richter, S. Ludewig, A. Winschel, T. Abel, C. Bold, L.R. Salzburger, S. Klein, K. Han, S.W. Weyer, A.K. Fritz, B. Laube, D.P. Wolfer, C.J. Buchholz, M. Korte, U.C. Müller, Distinct in vivo roles of secreted APP ectodomain variants APP α and APP β in regulation of spine density, synaptic plasticity, and cognition, *EMBO J.* 37 (2018) e201798335, doi:10.15252/emboj.201798335.
- [11] K.G. Ma, Y.H. Qian, Alpha 7 nicotinic acetylcholine receptor and its effects on Alzheimer's disease, *Neuropeptides* 73 (2019) 96–106, doi:10.1016/j.neurope.2018.12.003.
- [12] A.V. Terry Jr., P.M. Callahan, $\alpha 7$ nicotinic acetylcholine receptors as therapeutic targets in schizophrenia: Update on animal and clinical studies and strategies for the future, *Neuropharmacology* 170 (2020) 108053, doi:10.1016/j.neuropharm.2020.108053.
- [13] E. Portelius, U. Andreasson, J.M. Ringman, K. Buerger, J. Daborg, P. Buchhave, O. Hansson, A. Harmsen, M.K. Gustavsson, E. Hanse, D. Galasko, H. Hampel, K. Blennow, H. Zetterberg, Distinct cerebrospinal fluid amyloid beta peptide signatures in sporadic and PSEN1 A431E-associated familial Alzheimer's disease, *Mol. Neurodegener.* 5 (2010) 2, doi:10.1186/1750-1326-5-2.
- [14] E. Portelius, A. Westman-Brinkmalm, H. Zetterberg, K. Blennow, Determination of beta-amyloid peptide signatures in cerebrospinal fluid using immunoprecipitation-mass spectrometry, *J. Proteome Res.* 5 (2006) 1010–1016, doi:10.1021/pr050475v.
- [15] C. Haass, M. Willem, Secreted APP modulates synaptic activity: A novel target for therapeutic intervention? *Neuron* 101 (2019) 557–559, doi:10.1016/j.neuron.2019.01.058.
- [16] J.A. Morrissey, B.G. Mockett, A. Singh, D. Kweon, S.M. Ohline, W.P. Tate, S.M. Hughes, W.C. Abraham, A C-terminal peptide from secreted amyloid precursor protein- α enhances long-term potentiation in rats and a transgenic mouse model of Alzheimer's disease, *Neuropharmacology* 157 (2019) 107670, doi:10.1016/j.neuropharm.2019.107670.
- [17] D. Anni, E.M. Weiss, D. Guhathakurta, Y.E. Akdas, J. Klueva, S. Zeitler, M. Andres-Alonso, T. Huth, A. Fejtova, A β 1-16 controls synaptic vesicle pools at excitatory synapses via cholinergic modulation of synapsin phosphorylation, *Cell. Mol. Life Sci.* 78 (2021) 4973–4992, doi:10.1007/s00018-021-03835-5.
- [18] X. Gao, Y. Guan, C. Wang, M. Jia, S. Ahmad, M.F. Nouman, H. Ai, Specific interaction from different A β 42 peptide fragments to $\alpha 7nAChR$: A study of molecular dynamics simulation, *J. Mol. Model.* 30 (2024) 233, doi:10.1007/s00894-024-06032-w.

- [19] C.M. Novello, A. Gharpure, N. Mukhtasimova, R. Cabuco, L. Baxter, D. Borek, S.M. Sine, R.E. Hibbs, Structure and gating mechanism of the $\alpha 7$ nicotinic acetylcholine receptor, *Cell* 184 (2021) 2121–2134.e13, doi:10.1016/j.cell.2021.02.049.
- [20] S.M. Burke, M. Avstrikova, C.M. Novello, N. Mukhtasimova, J.P. Changeux, G.A. Thakur, S.M. Sine, M. Cecchini, R.E. Hibbs, Structural mechanisms of $\alpha 7$ nicotinic receptor allosteric modulation and activation, *Cell* 187 (2024) 1160–1176.e21, doi:10.1016/j.cell.2024.01.032.
- [21] Y. Zhao, S. Liu, Y. Zhou, M. Zhang, H. Chen, H. Xu, D. Sun, L. Liu, C. Tian, Structural basis of human $\alpha 7$ nicotinic acetylcholine receptor activation, *Cell Res.* 31 (2021) 713–716, doi:10.1038/s41422-021-00509-6.
- [22] D. Bertrand, C.H. Lee, D. Flood, F. Marger, D. Donnelly-Roberts, Therapeutic potential of $\alpha 7$ nicotinic acetylcholine receptors, *Pharmacol. Rev.* 67 (2015) 1025–1073, doi:10.1124/pr.113.008581.
- [23] H.R. Arias, Localization of agonist and competitive antagonist binding sites on nicotinic acetylcholine receptors, *Neurochem. Int.* 36 (2000) 595–645, doi:10.1016/s0197-0186(99)00154-0.
- [24] G.T. Young, R. Zwart, A.S. Walker, E. Sher, N.S. Millar, Potentiation of $\alpha 7$ nicotinic acetylcholine receptors via an allosteric transmembrane site, *Proc. Natl. Acad. Sci. U.S.A.* 105 (2008) 14686–14691, doi:10.1073/pnas.0804372105.
- [25] C. Stokes, M. Treinin, R.L. Papke, Looking below the surface of nicotinic acetylcholine receptors, *Trends Pharmacol. Sci.* 36 (2015) 514–523, doi:10.1016/j.tips.2015.05.002.
- [26] N. Andersen, J. Corradi, S.M. Sine, C. Bouzat, Stoichiometry for activation of neuronal $\alpha 7$ nicotinic receptors, *Proc. Natl. Acad. Sci. U.S.A.* 110 (2013) 20819–20824, doi:10.1073/pnas.1315775110.
- [27] V. Echeverria, A. Yarkov, G. Aliev, Positive modulators of the $\alpha 7$ nicotinic receptor against neuroinflammation and cognitive impairment in Alzheimer's disease, *Prog. Neurobiol.* 144 (2016) 142–157, doi:10.1016/j.pneurobio.2016.01.002.
- [28] T.L. Wallace, T.M. Ballard, B. Pouzet, W.J. Riedel, J.G. Wettstein, Drug targets for cognitive enhancement in neuropsychiatric disorders, *Pharmacol. Biochem. Behav.* 99 (2011) 130–145, doi:10.1016/j.pbb.2011.03.022.
- [29] N.S. Philip, L.L. Carpenter, A.R. Tyrka, L.H. Price, Nicotinic acetylcholine receptors and depression: A review of the preclinical and clinical literature, *Psychopharmacology* 212 (2010) 1–12, doi:10.1007/s00213-010-1932-6.
- [30] P. Dasgupta, W. Rizwani, S. Pillai, R. Kinkade, M. Kovacs, S. Rastogi, S. Banerjee, M. Carless, E. Kim, D. Coppola, E. Haura, S. Chellappan, Nicotine induces cell proliferation, invasion and epithelial-mesenchymal transition in a variety of human cancer cell lines, *Int. J. Cancer* 124 (2009) 36–45, doi:10.1002/ijc.23894.
- [31] R. Kandimala, P.H. Reddy, Therapeutics of neurotransmitters in Alzheimer's disease, *J. Alzheimer's Dis.* 57 (2017) 1049–1069, doi:10.3233/jad-161118.
- [32] E. Cecon, J. Dam, M. Luka, G. Gautier, A.M. Chollet, P. Delagrangue, L. Danober, R. Jockers, Quantitative assessment of oligomeric amyloid β peptide binding to $\alpha 7$ nicotinic receptor, *Br. J. Pharmacol.* 176 (2019) 3475–3488, doi:10.1111/bph.14688.
- [33] H.Y. Wang, D.H. Lee, M.R. D'Andrea, P.A. Peterson, R.P. Shank, A.B. Reitz, Beta-amyloid(1–42) binds to $\alpha 7$ nicotinic acetylcholine receptor with high affinity: Implications for Alzheimer's disease pathology, *J. Biol. Chem.* 275 (2000) 5626–5632, doi:10.1074/jbc.275.8.5626.
- [34] H.Y. Wang, D.H. Lee, C.B. Davis, R.P. Shank, Amyloid peptide A β (1–42) binds selectively and with picomolar affinity to $\alpha 7$ nicotinic acetylcholine receptors, *J. Neurochem.* 75 (2000) 1155–1161, doi:10.1046/j.1471-4159.2000.0751155.x.
- [35] Q. Liu, H. Kawai, D.K. Berg, Beta-amyloid peptide blocks the response of $\alpha 7$ containing nicotinic receptors on hippocampal neurons, *Proc. Natl. Acad. Sci. U.S.A.* 98 (2001) 4734–4739, doi:10.1073/pnas.081553598.
- [36] L. Pym, M. Kemp, V. Raymond-Delpech, S. Buckingham, C.A. Boyd, D. Sattelle, Subtype-specific actions of beta-amyloid peptides on recombinant human neuronal nicotinic acetylcholine receptors ($\alpha 7$, $\alpha 4\beta 2$, $\alpha 3\beta 4$) expressed in *Xenopus laevis* oocytes, *Br. J. Pharmacol.* 146 (2005) 964–971, doi:10.1038/sj.bjp.0706403.
- [37] H.R. Parri, C.M. Hernandez, K.T. Dineley, Research update: $\alpha 7$ nicotinic acetylcholine receptor mechanisms in Alzheimer's disease, *Biochem. Pharmacol.* 82 (2011) 931–942, doi:10.1016/j.bcp.2011.06.039.
- [38] K.H. Forest, N. Alfuraij, K. Arora, R. Taketa, T. Sherrin, C. Todorovic, J.L.M. Lawrence, G.T. Yoshikawa, H.L. Ng, V.J. Hruba, R.A. Nichols, Protection against β -amyloid neurotoxicity by a non-toxic endogenous N-terminal β -amyloid fragment and its active hexapeptide core sequence, *J. Neurochem.* 144 (2018) 201–217, doi:10.1111/jnc.14257.
- [39] M. Lasala, C. Fabiani, J. Corradi, S. Antollini, C. Bouzat, Molecular modulation of human $\alpha 7$ nicotinic receptor by amyloid- β peptides, *Front. Cell. Neurosci.* 13 (2019) 37, doi:10.3389/fncel.2019.00037.
- [40] M.L. Giuffrida, F. Caraci, B. Pignataro, S. Cataldo, P. De Bona, V. Bruno, G. Molinaro, G. Pappalardo, A. Messina, A. Palmigiano, D. Garozzo, F. Nicoletti, E. Rizzarelli, A. Copani, Beta-amyloid monomers are neuroprotective, *J. Neurosci.* 29 (2009) 10582–10587, doi:10.1523/jneurosci.1736-09.2009.
- [41] O. Hansson, S. Lehmann, M. Otto, H. Zetterberg, P. Lewczuk, Advantages and disadvantages of the use of the CSF amyloid β (A β) 42/40 ratio in the diagnosis of Alzheimer's disease, *Alzheimers Res. Ther.* 11 (2019) 34, doi:10.1186/s13195-019-0485-0.
- [42] L.W. Simpson, G.L. Szeto, H. Boukari, T.A. Good, J.B. Leach, Collagen hydrogel confinement of amyloid- β (A β) accelerates aggregation and reduces cytotoxic effects, *Acta Biomater* 112 (2020) 164–173, doi:10.1016/j.actbio.2020.05.030.
- [43] H. Li, E. Huang, Y. Zhang, S.Y. Huang, Y. Xiao, HDCK update for modeling protein-RNA/DNA complex structures, *Protein Sci* 31 (2022) e4441, doi:10.1002/pro.4441.
- [44] J. Lee, X. Cheng, J.M. Swails, M.S. Yeom, P.K. Eastman, J.A. Lemkul, S. Wei, J. Buckner, J.C. Jeong, Y. Qi, S. Jo, V.S. Pande, D.A. Case, C.L. Brooks III, A.D. MacKerell Jr., J.B. Klauda, W. Im, CHARMM-GUI input generator for NAMD, GROMACS, AMBER, OpenMM, and CHARMM/OpenMM simulations using the CHARMM36 additive force field, *J. Chem. Theory Comput.* 12 (2016) 405–413, doi:10.1021/acs.jctc.5b00935.
- [45] W.L. Jorgensen, J.D. Madura, Quantum and statistical mechanical studies of liquids. 25. Solvation and conformation of methanol in water, *J. Am. Chem. Soc.* 105 (1983) 1407–1413, doi:10.1021/ja00344a001.
- [46] W.G. Hoover, Canonical dynamics: Equilibrium phase-space distributions, *Phys. Rev. A* 31 (1985) 1695–1697, doi:10.1103/PhysRevA.31.1695.
- [47] J.R. Ray, A. Rahman, Statistical ensembles and molecular dynamics studies of anisotropic solids. II, *J. Chem. Phys.* 82 (1985) 4243–4247, doi:10.1063/1.448813.
- [48] N. Ojaghlo, J. Airas, L.M. McRae, C.A. Taylor, B.R. Miller III, C.A. Parish, Understanding the structure and apo dynamics of the functionally active JIP1 fragment, *J. Chem. Inf. Model.* 61 (2021) 324–334, doi:10.1021/acs.jcim.0c01008.
- [49] B. Hess, H. Bekker, H.J.C. Berendsen, J.G.E.M. Fraaije, LINCS: A linear constraint solver for molecular simulations, *J. Comput. Chem.* 18 (1997) 1463–1472, doi:10.1002/(SICI)1096-987X(199709)18:12<1463::AID-JCC4>3.0.CO;2-H.
- [50] S. Miyamoto, P.A. Kollman, SETTLE: An analytical version of the SHAKE and RATTLE algorithm for rigid water models, *J. Comput. Chem.* 13 (1992) 952–962, doi:10.1002/jcc.540130805.
- [51] Y. Qiu, A. Mekkat, H. Yu, S. Yigit, S. Hamaia, R.W. Farndale, D.L. Kaplan, Y.S. Lin, B. Brodsky, Collagen Gly missense mutations: Effect of residue identity on collagen structure and integrin binding, *J. Struct. Biol.* 203 (2018) 255–262, doi:10.1016/j.jsb.2018.05.003.
- [52] G. Bussi, D. Donadio, M. Parrinello, Canonical sampling through velocity rescaling, *J. Chem. Phys.* 126 (2007) 014101, doi:10.1063/1.2408420.
- [53] T. Zeiske, K.A. Stafford, R.A. Friesner, A.G. Palmer 3rd, Starting-structure dependence of nanosecond timescale intersubstrate transitions and reproducibility of MD-derived order parameters, *Proteins* 81 (2013) 499–509, doi:10.1002/prot.24209.
- [54] J. Huang, S. Rauscher, G. Nawrocki, T. Ran, M. Feig, B.L. de Groot, H. Grubmüller, A.D. MacKerell, CHARMM36m: An improved force field for folded and intrinsically disordered proteins, *Nat. Methods* 14 (2017) 71–73, doi:10.1038/nmeth.4067.
- [55] M.F. Adams, K.L. Linnemann, S.N. Bolz, F. Kaiser, S. Salentin, V.J. Haupt, M. Schroeder, PLIP 2021: Expanding the scope of the protein-ligand interaction profiler to DNA and RNA, *Nucleic Acids Res.* 49 (2021) W530–W534, doi:10.1093/nar/gkab294.
- [56] Y. Wang, Y. Liu, Y. Zhang, G. Wei, F. Ding, Y. Sun, Molecular insights into the oligomerization dynamics and conformations of amyloidogenic and non-amyloidogenic amylin from discrete molecular dynamics simulations, *Phys. Chem. Chem. Phys.* 24 (2022) 21773–21785, doi:10.1039/D2CP02851D.
- [57] O.S. Smart, J.G. Neduveilil, X. Wang, B.A. Wallace, M.S. Sansom, HOLE: A program for the analysis of the pore dimensions of ion channel structural models, *J. Mol. Graph. Model.* 14 (1996) 354–360, doi:10.1016/s0263-7855(97)00009-x.
- [58] E.F. Pettersen, T.D. Goddard, C.C. Huang, G.S. Couch, D.M. Greenblatt, E.C. Meng, T.E. Ferrin, UCSF Chimera—a visualization system for exploratory research and analysis, *J. Comput. Chem.* 25 (2004) 1605–1612, doi:10.1002/jcc.20084.
- [59] W. Humphrey, A. Dalke, K. Schulten, VMD: Visual molecular dynamics, *J. Mol. Graph.* 14 (1996) 33–38, doi:10.1016/0263-7855(96)00018-5.
- [60] R.E. Rigsby, A.B. Parker, Using the PyMOL application to reinforce visual understanding of protein structure, *Biochem. Mol. Biol. Educ.* 44 (2016) 433–437, doi:10.1002/bmb.20966.
- [61] R. Kumari, R. Kumar, A. Lynn, g_mmpbsa—a GROMACS tool for high-throughput MM-PBSA calculations, *J. Chem. Inf. Model.* 54 (2014) 1951–1962, doi:10.1021/ci500020m.
- [62] E. Wang, H. Sun, J. Wang, Z. Wang, H. Liu, J.Z.H. Zhang, T. Hou, Endpoint binding free energy calculation with MM/PBSA and MM/GBSA: Strategies and applications in drug design, *Chem. Rev.* 119 (2019) 9478–9508, doi:10.1021/acs.chemrev.9b00055.
- [63] Y.J. Sheng, Y.W. Yin, Y.Q. Ma, H.M. Ding, Improving the performance of MM/PBSA in protein-protein interactions via the screening electrostatic energy, *J. Chem. Inf. Model.* 61 (2021) 2454–2462, doi:10.1021/acs.jcim.1c00410.
- [64] K. Huang, S. Luo, Y. Cong, S. Zhong, J.Z.H. Zhang, L. Duan, An accurate free energy estimator: Based on MM/PBSA combined with interaction entropy for protein–ligand binding affinity, *Nanoscale* 12 (2020) 10737–10750, doi:10.1039/C9NR10638C.
- [65] B. Knapp, L. Ospina, C.M. Deane, Avoiding false positive conclusions in molecular simulation: The importance of replicas, *J. Chem. Theory Comput.* 14 (2018) 6127–6138, doi:10.1021/acs.jctc.8b00391.
- [66] P. Auffinger, E. Westhof, RNA hydration: Three nanoseconds of multiple molecular dynamics simulations of the solvated tRNA(Asp) anticodon hairpin, *J. Mol. Biol.* 269 (1997) 326–341, doi:10.1006/jmbi.1997.1022.
- [67] J. Chen, X. Liu, S. Zhang, J. Chen, H. Sun, L. Zhang, Q. Zhang, Molecular mechanism with regard to the binding selectivity of inhibitors toward FABP5 and FABP7 explored by multiple short molecular dynamics simulations and free energy analyses, *Phys. Chem. Chem. Phys.* 22 (2020) 2262–2275, doi:10.1039/C9CP05704H.
- [68] L.M. Espinoza-Fonseca, Molecular docking of four β -amyloid_{1–42} fragments on the $\alpha 7$ nicotinic receptor: Delineating the binding site of the A β peptides, *Biochem. Biophys. Res. Commun.* 323 (2004) 1191–1196, doi:10.1016/j.bbrc.2004.08.218.
- [69] D. Liu, J.V. de Souza, A. Ahmad, A.K. Bronowska, Structure, dynamics, and ligand recognition of human-specific CHRFAM7A (Dup $\alpha 7$) nicotinic receptor linked to neuropsychiatric disorders, *Int. J. Mol. Sci.* 22 (2021) 5466, doi:10.3390/ijms22115466.
- [70] T.M. Tong, K. Arora, M.M. White, R.A. Nichols, Role of key aromatic residues in the ligand-binding domain of $\alpha 7$ nicotinic receptors in the agonist action of beta-amyloid, *J. Biol. Chem.* 286 (2011) 34373–34381, doi:10.1074/jbc.M111.241299.
- [71] N.L. Puskar, X. Xiu, H.A. Lester, D.A. Dougherty, Two neuronal nicotinic acetylcholine receptors, $\alpha 4\beta 4$ and $\alpha 7$, show differential agonist binding modes, *J. Biol. Chem.* 286 (2011) 14618–14627, doi:10.1074/jbc.M110.206565.
- [72] N.A. Horenstein, T.J. McCormack, C. Stokes, K. Ren, R.L. Papke, Reversal of agonist selectivity by mutations of conserved amino acids in the binding site

- of nicotinic acetylcholine receptors, *J. Biol. Chem.* 282 (2007) 5899–5909, doi:[10.1074/jbc.M609202200](https://doi.org/10.1074/jbc.M609202200).
- [73] M. Nys, D. Kesters, C. Ulens, Structural insights into Cys-loop receptor function and ligand recognition, *Biochem. Pharmacol.* 86 (2013) 1042–1053, doi:[10.1016/j.bcp.2013.07.001](https://doi.org/10.1016/j.bcp.2013.07.001).
- [74] V. Bondarenko, M.M. Wells, Q. Chen, T.S. Tillman, K. Singewald, M.J. Lawless, J. Caporoso, N. Brandon, J.A. Coleman, S. Saxena, E. Lindahl, Y. Xu, P. Tang, Structures of highly flexible intracellular domain of human $\alpha 7$ nicotinic acetylcholine receptor, *Nat. Commun.* 13 (2022) 793, doi:[10.1038/s41467-022-28400-x](https://doi.org/10.1038/s41467-022-28400-x).
- [75] E. Cecon, J. Dam, M. Luka, C. Gautier, A.M. Chollet, P. Delagrangé, L. Danober, R. Jockers, Quantitative assessment of oligomeric amyloid β peptide binding to $\alpha 7$ nicotinic receptor, *Br. J. Pharmacol.* 176 (2019) 3475–3488, doi:[10.1111/bph.14688](https://doi.org/10.1111/bph.14688).
- [76] K.T. Dineley, K.A. Bell, D. Bui, J.D. Sweatt, β -amyloid peptide activates $\alpha 7$ nicotinic acetylcholine receptors expressed in *Xenopus* oocytes, *J. Biol. Chem.* 277 (2002) 25056–25061, doi:[10.1074/jbc.M200066200](https://doi.org/10.1074/jbc.M200066200).
- [77] R. Kaye, C.A. Lasagna-Reeves, Molecular mechanisms of amyloid oligomers toxicity, *J. Alzheimers Dis.* 33 (2013) S67–S78, doi:[10.3233/jad-2012-129001](https://doi.org/10.3233/jad-2012-129001).
- [78] W. Jongbloed, K.A. Bruggink, M.I. Kester, P.J. Visser, P. Scheltens, M.A. Blankenstein, M.M. Verbeek, C.E. Teunissen, R. Veerhuis, Amyloid- β oligomers relate to cognitive decline in Alzheimer's disease, *J. Alzheimers Dis.* 45 (2015) 35–43, doi:[10.3233/jad-142136](https://doi.org/10.3233/jad-142136).
- [79] E. Karran, B. De Strooper, The amyloid cascade hypothesis: Are we poised for success or failure? *J. Neurochem.* 139 (2016) 237–252, doi:[10.1111/jnc.13632](https://doi.org/10.1111/jnc.13632).
- [80] R.R. Sokal, F.J. Rohlf, *Biometry: The principles and Practice of Statistics in Biological Research*, 4th ed., W.H. Freeman, New York, 2012.
- [81] M.J. Thompson, F. Mansoub Bekarkhanechi, A. Ananchenko, H. Nury, J.E. Baenziger, A release of local subunit conformational heterogeneity underlies gating in a muscle nicotinic acetylcholine receptor, *Nat. Commun.* 15 (2024) 1803, doi:[10.1038/s41467-024-46028-x](https://doi.org/10.1038/s41467-024-46028-x).
- [82] A. Sethi, J. Eargle, A.A. Black, Z. Luthey-Schulten, Dynamical networks in tRNA: Protein complexes, *Proc. Natl. Acad. Sci. U.S.A.* 106 (2009) 6620–6625, doi:[10.1073/pnas.0810961106](https://doi.org/10.1073/pnas.0810961106).
- [83] J.R. López-Blanco, J.I. Aliaga, E.S. Quintana-Ortí, P. Chacón, iMODS: Internal coordinates normal mode analysis server, *Nucleic Acids Res.* 42 (2014) W271–W276, doi:[10.1093/nar/gku339](https://doi.org/10.1093/nar/gku339).
- [84] J.R. López-Blanco, J.I. Garzón, P. Chacón, iMod: Multipurpose normal mode analysis in internal coordinates, *Bioinformatics* 27 (2011) 2843–2850, doi:[10.1093/bioinformatics/btr497](https://doi.org/10.1093/bioinformatics/btr497).
- [85] J.A. Kovacs, P. Chacón, R. Abagyan, Predictions of protein flexibility: First-order measures, *Proteins* 56 (2004) 661–668, doi:[10.1002/prot.20151](https://doi.org/10.1002/prot.20151).